

The Planck-ATCA Co-eval Observations (PACO) project: the bright sample

Marcella Massardi^{1*}, Anna Bonaldi¹, Laura Bonavera^{2,3}, Marcos López-Cañiego⁴, Gianfranco De Zotti^{1,2}, Ronald D. Ekers³

¹*INAF, Osservatorio Astronomico di Padova, Vicolo dell'Osservatorio 5, I-35122 Padova, Italy*

²*SISSA, via Bonomea 265, I 34136 Trieste, Italy*

³*Australia Telescope National Facility, CSIRO Astronomy and Space Science, PO Box 76, Epping, NSW 1710, Australia*

⁴*Instituto de Física de Cantabria (CSIC-UC), Avda. los Castros s/n, 39005 Santander, Spain*

ABSTRACT

The Planck-ATCA Co-eval Observations (PACO) have provided flux density measurements at frequencies below and overlapping with Planck frequency bands of suitably chosen samples of AT20G radio sources, almost simultaneously with Planck observations. On the whole, we have observed with the Australia Telescope Compact Array (ATCA) 482 sources in the frequency range between 4.5 and 40 GHz in the period between July 2009 and August 2010. Several sources were observed more than once. In this paper we present the aims of the project, the selection criteria, and the observation and data reduction procedures. We also present the data in total intensity for a complete sample of 189 sources with $S_{20\text{GHz}} > 500$ mJy, Galactic latitude $|b| > 5^\circ$, and declination $\delta < -30^\circ$, and some statistical analysis of the spectral behaviour and variability of this sample, referred to as the “bright PACO sample”. These data are important to investigate confusion effects affecting Planck data on radio sources. On the other hand, compared with the CMB dipole-based calibrated flux densities measured by the Planck satellite, could be used to infer absolute calibrations for ground based telescopes. To this end, we also provide some test fluxes on bright calibrators.

Key words: galaxies: active – radio continuum: galaxies – radio continuum: general – cosmic microwave background.

1 INTRODUCTION

The ESA’s Planck satellite¹ is surveying the sky in nine frequency bands (33, 40, 70 GHz for the Low Frequency Instrument, LFI, and 100, 143, 217, 353, 545, 857 GHz for the High Frequency Instrument, HFI, with FWHM ranging from 33 to 5 arcmin). At the HFI frequencies it will provide the first all-sky surveys ever, while at LFI frequencies its higher sensitivity and resolution will allow a significant improvement over WMAP (López-Cañiego et al. 2006; Leach et al. 2008). Planck thus offers a unique opportunity to carry out an unbiased investigation of the spectral properties of radio sources in a poorly explored frequency range, partially inaccessible from the ground.

Clearly Planck’s science yields can be greatly increased by simultaneous (i.e. not affected by variability) ground based observations at lower frequencies as well as at frequencies overlapping with Planck channels. Simultaneous

observations at overlapping frequencies are important on one side to transfer Planck’s excellent flux density calibration, based on the CMB dipole, to the primary calibrators used by ground-based telescopes and, on the other side, to help with the validation of sources detected by Planck.

At present, the flux density scales are well determined for frequencies up to 20 GHz but there are known problems at the higher frequencies. The difficulty occurs because the radio interferometers, which can make the most precise flux density measurements at high frequencies, need point sources to calibrate and the strong point sources are highly variable AGNs. This has led to the use of the planets, Mars and Uranus, as primary calibrators. These planets are resolved at all but the shortest interferometer baselines at the higher frequencies and their flux densities are estimated using relatively complex atmospheric models. In the case of Uranus there is a further complication because of the known orbital change in flux density as our view changes from equatorial to polar during the Uranian year. Simultaneous observations of very bright sources give a unique opportunity to

* E-mail: marcella.massardi@oapd.inaf.it

¹ <http://sci.esa.int/science-e/www/area/index.cfm?fareaid=17>

tie all the high frequency flux density scales together with the Planck’s calibration.

On the other hand, source confusion is a serious issue for Planck, due to its rather large beam sizes. Sources near Planck’s detection limit may be strongly affected by the Edington’s (1913) bias that leads to systematic flux density overestimates (Hogg & Turner 1998). Also, confusion fluctuations may produce high intensity peaks that may be misinterpreted as real sources. Moreover, confusion can shift the positions of intensity peaks from the true source positions (Hogg 2001), complicating their identification. Simultaneous ground based observations, with much better resolution and signal-to-noise ratio will allow an accurate control of these effects.

A definition of sources Spectral Energy Distributions (SEDs) over a frequency range as large as possible is crucial in determining their physical properties and in identifying the different components that may contribute to their emission. Given that observations in the full Planck frequency range will not be repeatable at least in the foreseeable future, it is essential not to lose the occasion while Planck is flying.

Obviously, observations simultaneous with Planck can be planned only for previously known sources. The Australia Telescope 20 GHz (AT20G; Murphy et al. 2010; Massardi et al. 2010) survey provides the best sample for this purpose. This is the largest ground-based sample of the high radio frequency (> 10 GHz) sky: it is 93% complete above 100 mJy at 20 GHz over the whole Southern sky with follow-up (within a few weeks time) at 4.8 and 8.6 GHz. For typical source spectra (Massardi et al. 2008), it is somewhat deeper than Planck, that is expected to reach detection limits ranging from $\simeq 400$ mJy at 30 GHz to $\simeq 220$ mJy at 100 GHz (Leach et al. 2008).

The above considerations have motivated the Planck-ATCA Co-eval Observations (PACO) project, described in §2. The observations exploited the capabilities of the new Australia Telescope Compact Array Broadband Backend (CABB; Ferris & Wilson 2002) system between 4.5 and 40 GHz. In §3 we describe and discuss the data for the sub-sample of 189 sources with 20 GHz flux density $S_{20\text{GHz}} > 500$ mJy, Galactic latitude $|b| > 5^\circ$, and declination $\delta < -30^\circ$ (the “bright PACO sample”) drawn from the AT20G catalogue (Murphy et al. 2010). In §4 we provide some flux density values on calibrators which could be of use for cross-calibration tests once the Planck data will be available and discuss the fractional calibration error we can get from such exercise assuming the nominal Planck calibration quality. In §5 we summarize our findings.

2 THE PACO PROJECT

2.1 Sample selection

The PACO sample is a combination of several sub-samples selected in order to maximize the scientific outcome in the allocated time. The ATCA allows us to make observations at frequencies lower than or close to those of the lowest frequency Planck channels at 30 and 44 GHz. On the whole we have observed 482 AT20G extragalactic sources at Galactic latitude $|b| > 5^\circ$ and outside a 5° radius circle centered

at $\text{RA} = 80.8939^\circ, \delta = -69.7561^\circ$ (the LMC region). Of these, 344 sources form 3 partially overlapping complete sub-samples, selected for different purposes.

- The “faint PACO sample” is made of 162 sources with $S_{20\text{GHz}} > 200$ mJy in the southern ecliptic pole region (ecliptic latitude $< -75^\circ$) and with $3\text{h} < \text{RA} < 9\text{h}$, $\delta < -30^\circ$ (Bonavera et al. 2011). Near the ecliptic poles Planck’s scan circles intersect. Therefore the area is covered many times, and Planck’s sensitivity is maximal. Nevertheless, we expect that many sources in this sample will not be detected by Planck. On the other hand, Poisson fluctuations due to extragalactic sources below the detection limit (expected to be of 100–250 mJy in the range 100–353 GHz, Leach et al. 2008) are the main contaminant of Planck maps on angular scales smaller than $20' - 30'$ at frequencies of up to $\simeq 100$ GHz (Toffolatti et al. 1998, 1999; De Zotti et al. 1999). It is therefore important to characterize as accurately as possible radio sources down to below the Planck detection limits.

- The “spectrally-selected PACO sample” comprises the 69 sources with $S_{20\text{GHz}} > 200$ mJy and inverted or upturning spectra in the frequency range 5–20 GHz, selected over the whole southern sky (Massardi et al. 2011);

- The “bright PACO sample” comprising the 189 sources with $S_{20\text{GHz}} > 500$ mJy at $\delta < -30^\circ$, presented and discussed in this paper.

In addition we have observed a sample of the 63 brightest Southern sources included in a long-term (up to 15 years) monitoring program at various frequencies with the Swedish-ESO Submillimetre Telescope (SEST, Tornikoski et al. 1996) and observed also with the LABOCA instrument on the APEX. Based on a source counts analysis, this sample appears to be 91 per cent complete down to the cutoff of 1 Jy at 90 GHz. These sources are of special interest because some of them may be flaring during the Planck mission. If this happens, we get an unusually broad simultaneous frequency coverage of the flare.

The samples described above include 76 ATCA calibrators with 20 GHz flux density $S_{20\text{GHz}} > 200$ mJy that showed more than 10% variability at this frequency in the last three years. Further 121 variable ATCA calibrators were added to the PACO sample, so that their total observed number is of 197. Our data will also be included in the AT calibrator database.

Our observations allow us to characterize the source spectra in the range 4.5–40 GHz. Planck data will allow us to extend the spectral coverage up to 857 GHz, at least for the brightest flat-spectrum sources.

The classification as extragalactic objects and an indication of source extendedness up to 20 GHz were taken from the AT20G catalog. AT20G positions were also used unless more precise coordinates were available, as is the case, e.g., for the AT calibrators whose positions are based on VLBI observations. A map of our sample is shown in Fig. 1. As pointed out by Massardi et al. (2010) the sample may still contain some Galactic sources, but they should be very few because the relatively high resolution 20 GHz observations preferentially select compact objects (< 30 arcsec) and Galactic sources with $|b| > 1.5^\circ$ are rarely that small, especially at the brighter flux density levels.

Table 1. The 63 good weather observational runs for the PACO project between July 2009 and August 2010.

Date	array	Allocated time [h]	Frequency Range	Date	array	Allocated time [h]	Frequency Range
2009-07-09	H75C	8.5	4.5-40 GHz	2010-02-07	6A	4.5	4.5-25 GHz
2009-07-10	H75C	5	17-40 GHz	2010-02-14	6A	9	4.5-25 GHz
2009-07-16	H75C	2	4.5-25 GHz	2010-02-28	750B	8.5	4.5-40 GHz
2009-07-18	H75C	1	32-40 GHz	2010-03-02	750B	4	4.5-25 GHz
2009-07-25	H75C	8	4.5-40 GHz	2010-03-06	H168	10	4.5-40 GHz
2009-07-26	H75C	7	4.5-40 GHz	2010-03-15	H168	8	4.5-40 GHz
2009-07-31	1.5A	7	4.5-40 GHz	2010-04-01	6A	12	4.5-40 GHz
2009-08-09	6D	6.5	4.5-40 GHz	2010-04-06	6A	4	4.5-25 GHz
2009-08-13	6D	8	4.5-40 GHz	2010-04-10	6A	5	4.5-40 GHz
2009-08-24	6D	2.5	17-40 GHz	2010-04-11	6A	6.5	4.5-40 GHz
2009-08-25	6D	3.5	17-40 GHz	2010-04-23	6A	7	4.5-40 GHz
2009-08-30	6D	6	4.5-40 GHz	2010-04-24	6A	7	4.5-40 GHz
2009-09-15	H214	8	4.5-40 GHz	2010-05-01	6A	4	4.5-40 GHz
2009-09-26	H75	14	4.5-40 GHz	2010-05-03	6A	4	4.5-40 GHz
2009-09-29	H75	4	4.5-40 GHz	2010-05-11	H214	4	4.5-40 GHz
2009-10-07	H75	6.5	4.5-40 GHz	2010-05-18	6C	7	4.5-40 GHz
2009-10-14	H168	10	4.5-40 GHz	2010-05-30	6C	12	4.5-40 GHz
2009-10-28	1.5B	4	4.5-40 GHz	2010-06-05	6C	7.5	4.5-40 GHz
2009-10-29	1.5B	4	4.5-40 GHz	2010-06-11	6C	4	4.5-40 GHz
2009-11-06	1.5B	14.5	4.5-40 GHz	2010-06-14	6C	12	4.5-40 GHz
2009-11-11	6B	4	4.5-40 GHz	2010-06-19	6C	14.5	4.5-40 GHz
2009-11-19	6B	11	4.5-40 GHz	2010-07-02	6C	4	4.5-40 GHz
2009-11-24	6B	4	4.5-40 GHz	2010-07-12	1.5D	5.5	4.5-40 GHz
2009-12-04	EW352	14	4.5-40 GHz	2010-07-16	EW352	5	4.5-40 GHz
2009-12-07	EW352	13	4.5-40 GHz	2010-07-31	H168	4	4.5-40 GHz
2009-12-17	6A	9.5	4.5-40 GHz	2010-08-10	H168	6	4.5-40 GHz
2009-12-29	6A	8	4.5-40 GHz	2010-08-13	H168	2	32-40 GHz
2010-01-03	6A	4.5	4.5-25 GHz	2010-08-14	H168	6.5	4.5-40 GHz
2010-01-17	6A	4	4.5-25 GHz	2010-08-15	H168	6.5	4.5-40 GHz
2010-01-24	6A	7	4.5-40 GHz	2010-08-20	H168	10	4.5-40 GHz
2010-01-27	6A	4	4.5-25 GHz	2010-08-21	H168	10	4.5-40 GHz
2010-02-06	6A	12	4.5-25 GHz				

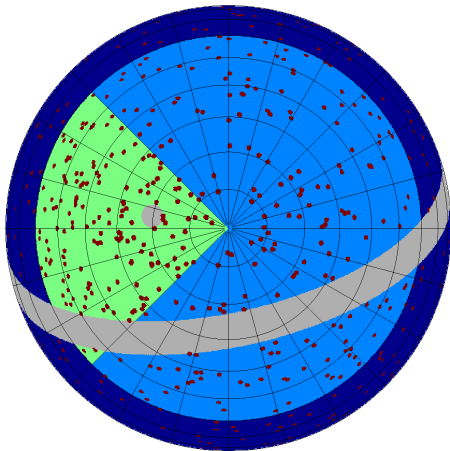


Figure 1. Orthographic projection of the southern sky, showing the distribution of the PACO samples (RA=0h is at the top and the RA increases counterclockwise). The grey area shows the Galactic cut and the 5° radius circle surrounding the center of the LMC. Sources in these regions were excluded from the PACO samples. Sources within the green region [$3 < RA < 9\text{hr}$, $\delta < -30^\circ$] are those included in the faint PACO sample. The bright PACO sample covers the whole area at $\delta < -30^\circ$. The spectrally-selected sample and the other sources are spread over the whole southern sky (excluding, as always, the grey area).

2.2 Observations

The Planck scanning strategy has been publicly released soon after the satellite launch. The satellite scans the sky in circles passing close to the ecliptic poles. All Planck receivers cross any given position in the sky within a few days for sources lying on the ecliptic equator. Sources close to the ecliptic poles remain within the satellite focal plane for up to 2.5 months. The satellite covers the whole sky in about 6 months. Because the maps are the result of averaging all the scans through a position, we can't get information from them on the very short term variability. Variability tests on the time ordered data are limited to the brightest object because of lack of integration on source. We consider observations to be 'co-eval' with the satellite if performed within 10 days from the satellite observations at any of its LFI frequencies. The Planck-On-the Flight forecaster (Massardi & Burigana 2010) has been developed and used to predict when the PACO sources are observed by the satellite, according to its pre-programmed pointing lists and the focal plane properties.

The new ATCA CABB system allows 2×2 GHz simultaneous bands in continuum. Applied to the 6×22 m ATCA antennas it gives a noise level of 0.5 mJy in 1 min on source in the 7 mm band. We chose to use the receivers at 7 mm (intermediate frequencies, IFs, at 33 and 39 GHz), to over-

lap the lower-frequency Planck channels, at 12 mm (IFs at 18 and 24 GHz) to overlap our selection frequency, and at 3-6 cm (IFs at 5.5 and 9 GHz) to extend the SEDs to lower frequencies.

The selection within the AT20G catalogue guarantees that most radio sources have small angular sizes so that the particular configuration of the ATCA is not crucial for flux density estimation. Hybrid arrays are preferable for equatorial sources, for which the beam shape of EW arrays is elongated. Because of the risk of contamination within the highly distorted beam, sources with declination $\delta > -10^\circ$ have not been observed at 3-6 cm.

The scheduling process tries to reconcile the limits set by the allocated local sidereal time (LST) ranges (varying according to the Planck scanning strategy) and by the array configuration in use, aiming at minimizing the slewing time, to maximize the time on source and to complete the measurements at the selected frequencies (i.e. including considerations about the weather and the minimization of the band switches).

For each epoch and each frequency, a very bright compact object is used for bandpass calibration. Observations of the bandpass are usually repeated several times to account for time instability of the band. PKS B1934-638 is the primary calibrator for all the frequencies. At 7 mm we have sometimes observed Uranus. From the comparisons of the two sources that have been performed in several epochs, we estimate that the model for Uranus requires a flux density correction by a factor of ~ 0.82 at 33 GHz and ~ 0.84 at 39 GHz, that is in agreement with what estimated on the basis of the on-going calibrator model update (J. Stevens, priv. comm.). Hence we applied these correction factors to all the 7 mm flux densities calibrated with the planet.

A leakage calibrator selected among the polarized objects of the AT20G (a bright point-like unpolarized one should work as well) is observed at least 3 times, better if across the transit of the source, at each frequency for almost all the observing runs. Pointing calibration is performed regularly for 12 and 7 mm observations. Each source at each frequency is observed for 1.5 min in a single pointing.

Thanks to the compactness of most of the PACO sources neither imaging nor phase calibration is necessary, but since sources are self-calibrated we get good images when observing with hybrid arrays. We got a suitable flux density estimation from the visibilities using the triple-correlation techniques, as will be explained in the next sections.

The project got ~ 450 hours allocated over 65 epochs between July 2009 and August 2010 (i.e. during the time when Planck completed two all-sky surveys). 2 epochs have been discarded for bad weather. Because of the high sensitivity in total intensity and the brightness of the sources in our sample we could observe on average 20 objects per run at all the 3 pairs of frequencies. Bad weather seriously affected some of the Austral summer epochs making it impossible to get the 7 mm data in a few runs. Table 1 summarizes the configurations, and frequencies observed in each run.

2.3 Data reduction

Data reduction is performed by a C-shell coded pipeline which uses tasks from the MIRIAD software package (Sault

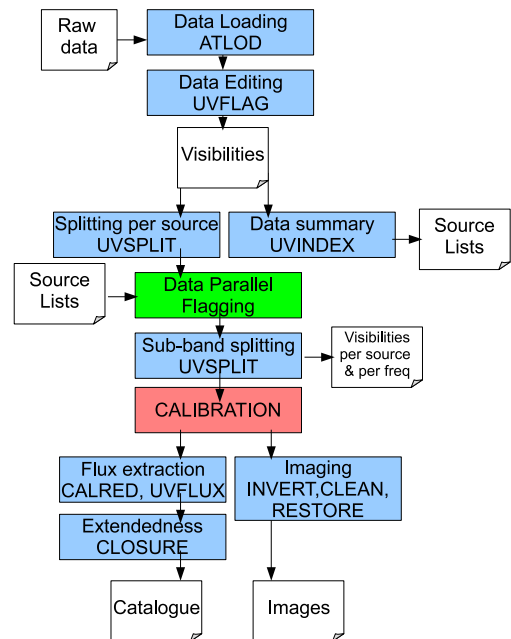


Figure 2. Data reduction pipeline diagram. In capital letters are the Miriad tasks used.

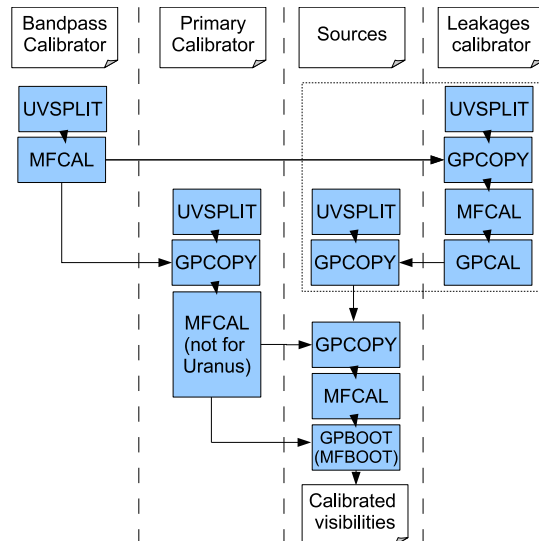


Figure 3. Calibration scheme. The indications in parenthesis refer to the case of Uranus as primary calibrator. The steps included in the dotted square have been applied only when a suitable leakage calibrator has been observed.

et al. 1995) according to the scheme in Fig. 2. Chunks of data affected by bad weather conditions or instrumental malfunction are removed, as well as data affected by shadowing or known radio interference. Automatic procedures identify among the 2048 channels which constitute the 2.048 GHz bandwidth for each IF, those that exceed by 5σ the mean value for each baseline for each source. Typically less than 1% of the band is flagged. In order to properly define the

detailed source spectral behaviour we have split each 2 GHz band into 4×512 MHz sub-bands, and calibrated each sub-band independently. As a drawback, we lost a factor of 2 in the S/N ratio per sub-band. The steps for calibration are plotted in Fig. 3.

2.3.1 Source extendedness

We expect that the AT20G analysis for extendedness already identifies all the extended sources up to 20 GHz. We have therefore done the analysis only for the 7 mm data, applying the automatic procedure to distinguish between point-like and extended sources used by Massardi et al. (2008) for the AT20G bright sample.

The positional error of the AT20G sources has been found to be $\Delta \text{RA} = 0.9''$ and $\Delta \delta = 1.0''$ (Murphy et al. 2010) for point sources. The pointing accuracy of the ATCA at any of our observing frequency is less than an arcsec. Hence, the visibility pattern is constant for point sources, and is a Gaussian peaking in the phase center for the extended objects, if we assume that we are pointing to the source center.

The ratio between the actual and the theoretical phase closure rms calculated accounting for the noise in the beam gives an indication on whether the source is extended. For a point source the phase closure rms should be zero and is independent of instrumental effects. When the ratio of actual to theoretical phase closure rms is larger than 3 the source should be considered extended. We have used this ratio as an indication of extendedness for the sources that appear to be extended at 7mm and were not identified as extended in the AT20G catalogue.

2.3.2 Flux density estimation

To estimate the flux densities for point sources we have used the triple product (i.e. the geometrical average of the amplitude over a closure triangle averaged over all the possible triangles, given by the MIRIAD task CALRED). Both the AT20G and our flux density estimation techniques are well suited for point sources. On the other hand, for the 30 m spacing used for the blind survey, the amplitude is underestimated by 50% in the case of sources larger than 45 arcsec. Therefore a different technique must be used to estimate their flux densities; we adopted the amplitude of the shortest spacings (given by the MIRIAD task UVFLUX) as the best flux estimator. This approach still underestimates the flux densities for sources more extended than $15(100\text{m}/b_{\text{min}})(39\text{GHz}/\nu)$ arcsec, where b_{min} is the shortest baseline for any used configuration. Thus our samples are increasingly incomplete for more and more extended sources. Table 2 lists the shortest baselines (b_{min}), and the primary and synthesized beam sizes for the central frequencies of our observing runs for all the array configurations used.

The noise term of the flux density errors for point sources are calculated as the rms of the triple product amplitudes over all the possible triangles of antennas. For extended sources the rms of the triple product has been multiplied by $\sqrt{n_b}$ where n_b is the number of baselines of the used configuration. An analysis of the gain term of the flux density error including systematics and calibration uncertainties is discussed in § 2.4.1.

2.4 Quality assessment of the results

By running the data reduction pipeline previously described we have generated a preliminary catalogue for each observing epoch. This catalogue was then processed through a quality assessment procedure. Depending on the results of the assessment, we either proceeded to create the final catalogue for the considered epoch or we carried out further investigations in order to improve the results.

The quality assessment step is needed because each observation can be affected by different problems (bad weather conditions, some antenna correlations to be rejected, residual spikes, etc.) which could not be addressed by the automatic pipeline. It is designed to identify the major flaws the catalogue of each observing epoch may have and to perform an a-posteriori flagging of the bad data.

The quality check assumes that the true SEDs do not contain discontinuities; those observed are interpreted as due to residual spikes in the data or to calibration errors. The smoothness of the spectra is checked by comparing the data points with a fitting polynomial function with degree equal to the number of 2 GHz bands observed. We stress that, at this stage, the fit is done for flagging purposes only.

We discard the data points with a fractional divergence from the fitting line larger than 4σ , where σ is the smallest between the rms fractional divergence of the other points and 0.02, corresponding to $\sim 2\times$ the maximum in the distribution of the rms fractional divergences for all the observing epochs. Whenever two data points within the same 2 GHz band are discarded, it is likely that some problems are affecting the whole band, and we flag it for the considered source.

When the fraction of good data for a given observing epoch exceeds 90% (and this happens in most cases) we directly create the final catalogue of the unflagged data. All the other cases are inspected in order to identify the problems and new runs of the data reduction pipeline with improved specifications are performed until satisfactory results are reached. The recovery succeeded in most cases. The exceptions are those in which some problems affected the observation of the flux density calibrator for some bands. In a few cases the calibrator couldn't be recovered to a satisfactory level and the whole target sample was rejected. After the quality assessment process, we are left with more than 85% of our data.

2.4.1 Flux density error estimation

The gain term of the noise for each epoch was estimated as the rms fractional divergence between the data and the fit, re-calculated as discussed in the previous section after all the flagged data have been removed. For the days with less than 10 good fits available we have used $\sigma_g = 0.012$ equal to the median of the rms fractional divergence calculated over all the epochs. Hence, the final error bars for each point-source in each epoch have been estimated as square root of the square of the gain term multiplied by the source flux density plus the square of noise term (estimated as discussed in 2.3.2). Since our flux density estimation techniques are not well suited for extended sources, we have increased their gain term used in the error estimate to a minimum of 5 per cent of their flux density.

Table 2. The array configurations and their resolution properties.

Array Configuration	Shortest Baseline [m]	frequency IF1 - IF2[GHz]	Primary beam FWHM [arcmin]	Beam IF1 [arcsec]	Beam IF2 [arcsec]	D_{\max} [arcmin]
H75c	31 (1-4,2-4)	5.5 - 9	8.7 - 5.3	115.51 x 115.51	70.59 x 70.59	6.0 - 3.7
		18 - 24	2.6 - 2.0	35.29 x 35.29	26.47 x 26.47	1.8 - 1.4
		33 - 39	1.5 - 1.2	19.25 x 19.25	16.29 x 16.29	1.0 - 0.9
H168d	61 (1-4,2-4)	5.5 - 9	8.7 - 5.3	50.23 x 50.23	30.69 x 30.69	3.1 - 1.9
		18 - 24	2.6 - 2.0	15.35 x 15.35	11.51 x 11.51	0.9 - 0.7
		33 - 39	1.5 - 1.2	8.37 x 8.37	7.08 x 7.08	0.5 - 0.4
H214c	82 (2-4)	5.5 - 9	8.7 - 5.3	38.9 x 38.9	23.78 x 23.78	2.3 - 1.4
		18 - 24	2.6 - 2.0	11.89 x 11.89	8.92 x 8.92	0.7 - 0.5
		33 - 39	1.5 - 1.2	6.48 x 6.48	5.49 x 5.49	0.4 - 0.3
1.5A	153 (1-2)	5.5 - 9	8.7 - 5.3	7.2 x 8.31	4.4 x 5.08	1.2 - 0.7
		18 - 24	2.6 - 2.0	2.2 x 2.54	1.65 x 1.91	0.4 - 0.3
		33 - 39	1.5 - 1.2	1.2 x 1.39	1.02 x 1.17	0.2 - 0.2
1.5B	31 (1-2)	5.5 - 9	8.7 - 5.3	7.2 x 8.31	4.4 x 5.08	6.0 - 3.7
		18 - 24	2.6 - 2.0	2.2 x 2.54	1.65 x 1.91	1.8 - 1.4
		33 - 39	1.5 - 1.2	1.2 x 1.39	1.02 x 1.17	1.0 - 0.9
6B	214 (4-5)	5.5 - 9	8.7 - 5.3	2.48 x 2.86	1.51 x 1.75	0.9 - 0.5
		18 - 24	2.6 - 2.0	0.76 x 0.87	0.57 x 0.65	0.3 - 0.2
		33 - 39	1.5 - 1.2	0.41 x 0.48	0.35 x 0.4	0.1 - 0.1
6D	77 (4-5)	5.5 - 9	8.7 - 5.3	2.48 x 2.86	1.51 x 1.75	2.4 - 1.5
		18 - 24	2.6 - 2.0	0.76 x 0.87	0.57 x 0.65	0.7 - 0.6
		33 - 39	1.5 - 1.2	0.41 x 0.48	0.35 x 0.4	0.4 - 0.3

The gain term does not include any bias due to absolute calibration errors which should affect equally all the frequencies calibrated with the same calibrator source (generally PKS 1934-638). The comparison with Planck CMB-dipole calibrated flux densities will allow us to estimate this bias and correct it.

3 THE BRIGHT SOURCES PACO CATALOGUE

Of the 189 sources comprised in the PACO bright sample, 13 are flagged as extended in the AT20G catalog and 2 more (J062706-352916 and J130527-492804) were found to be extended by our 7mm data analysis. Two of the 13 AT20G extended sources (J051926-454554 and J051949-454643) correspond to the core and to the western lobe of Pictor A. We have performed a dedicated observation in total intensity and polarization at 18, 24, 33 and 39 GHz of this well-known extended radio source by mosaicking the region including the core and the western lobe, which is the brightest and the more highly polarized (Burke-Spolaor et al. 2009). These observations will be presented in a separate paper and the two sources have been left aside.

After the data reduction, 7 extended sources (J040848-750720, J084127-754028, J130527-492804, J161505-605427, J193557-462043, J195817-550923, J235904-605503) turned out to have unreliable flux density estimates at all the frequencies and for all the days of observations. This is mostly due to the fact that the observations were run with too extended array configurations, so that the sensitivity on the observed scale was poor. They have been therefore not included in the present catalogue.

For all the other extended objects (J052257-362730, J062706-352916, J074331-672625, J114531-483610, J132527-430104, J215706-694123) the estimated flux densities are

lower limits to the integrated flux densities. Since these sources passed all the quality checks they have been included in the catalogue, with flux densities listed as lower limits, but have been excluded from further analysis.

Because of the too large size of the table, the catalogue of the 180 sources for which we have a flux density estimation or a lower limit is available only online. Columns are as follows:

- 1 AT20G name;
- 2-3 J2000 equatorial coordinates;
- 4 epoch of observation as [yymmdd];
- 5 flag 's' for simultaneity within 10 days from the Planck observations. The epochs before February 2010 have to be compared with the first Planck survey, whereas the following epochs should be compared with the second Planck survey.
- 6 flag 'e' for extended sources;
- 7-31 flux densities in mJy at the 24 frequencies between 4732 and 39768 MHz in which our 6×2-GHz bands have been divided;
- 32-55 flux density errors;
- 56-60 fit parameters, S_0 , ν_0 , a , b (see §3.1).

Figure 4 shows the spectra for the point-like sources in the PACO bright sample. Different colours (in the on-line version of the plot only) correspond to different observing epochs. Figure 5 shows some of the images for each frequency for one of our point sources: for the epochs observed with hybrid arrays good quality images could be obtained even if we observe only one cut per source. This is possible thanks to the brightness of the sources in our sample. It is a clear indication of the quality of our observations and of the beam size at the different frequencies.

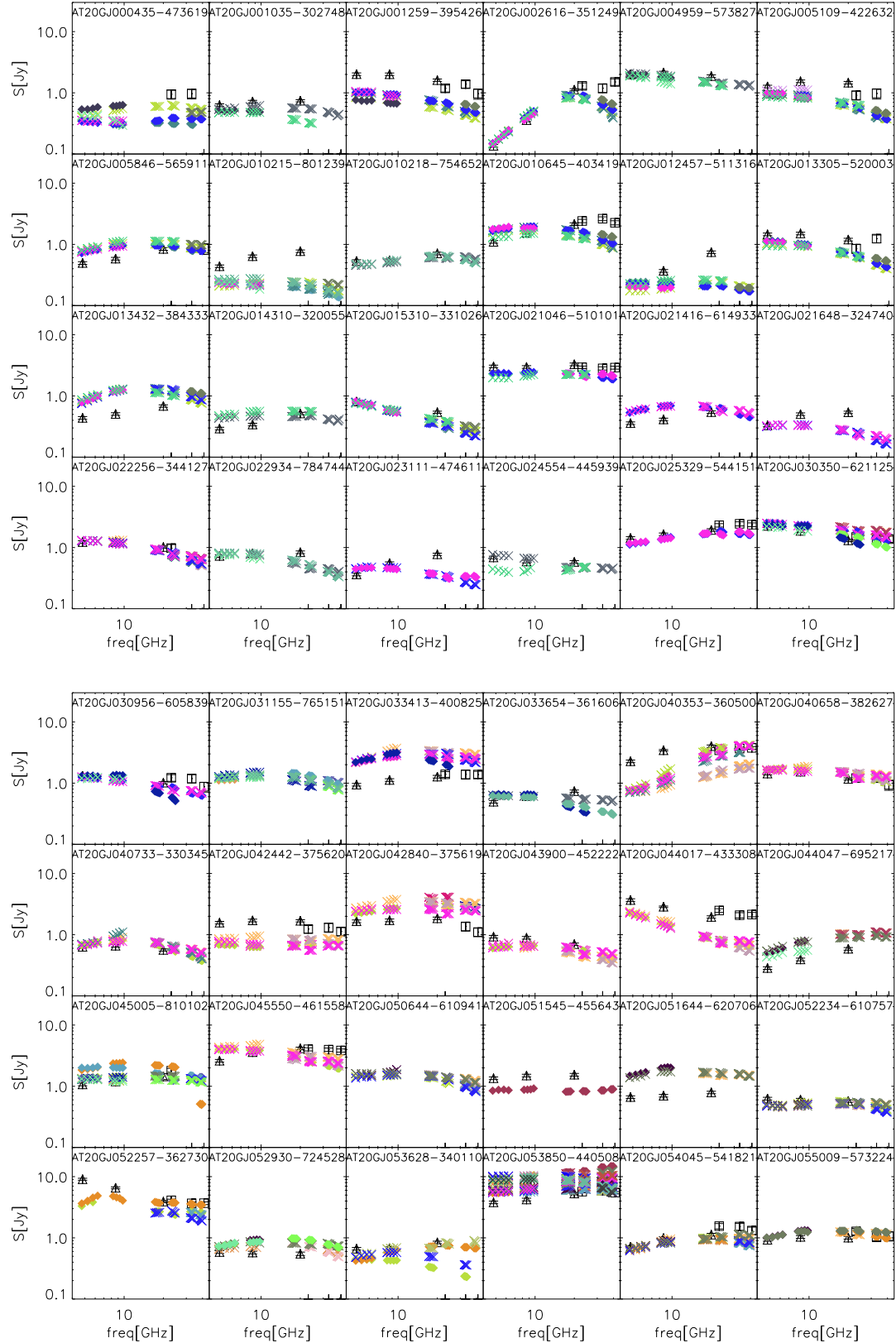


Figure 4. Spectra of point-like sources in the PACO bright sample (asterisks). Different colours correspond to different observing epochs. Diamonds corresponds to epochs simultaneous to Planck observations. To avoid overcrowding we have not plotted the error bars that are in all cases smaller than the symbol size. Also shown, for comparison, are the AT20G data (triangles) and, when available, WMAP data taken from the NEWPS_5yr catalog (squares; Massardi et al. 2009).

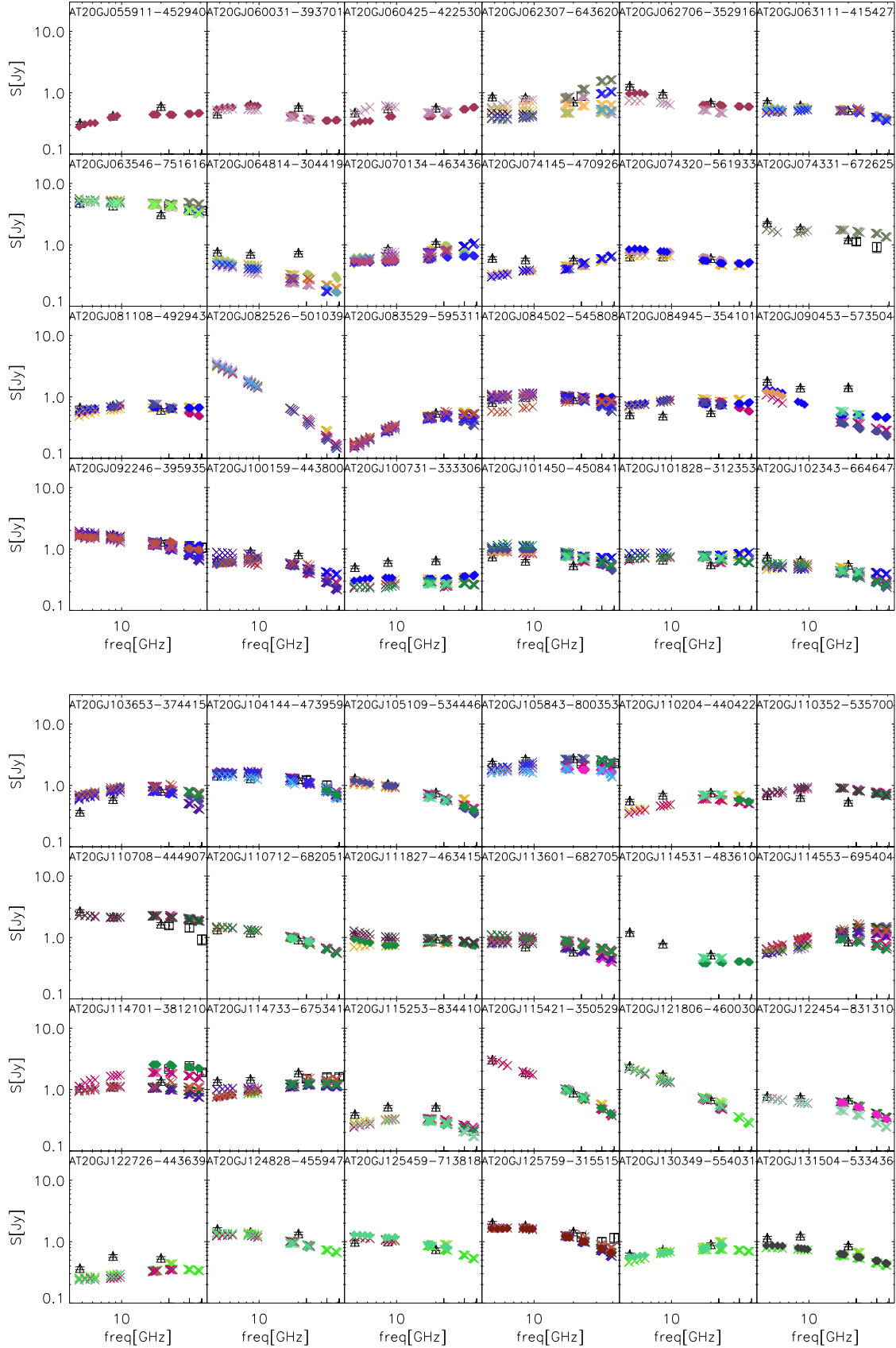


Figure 4. Continue.

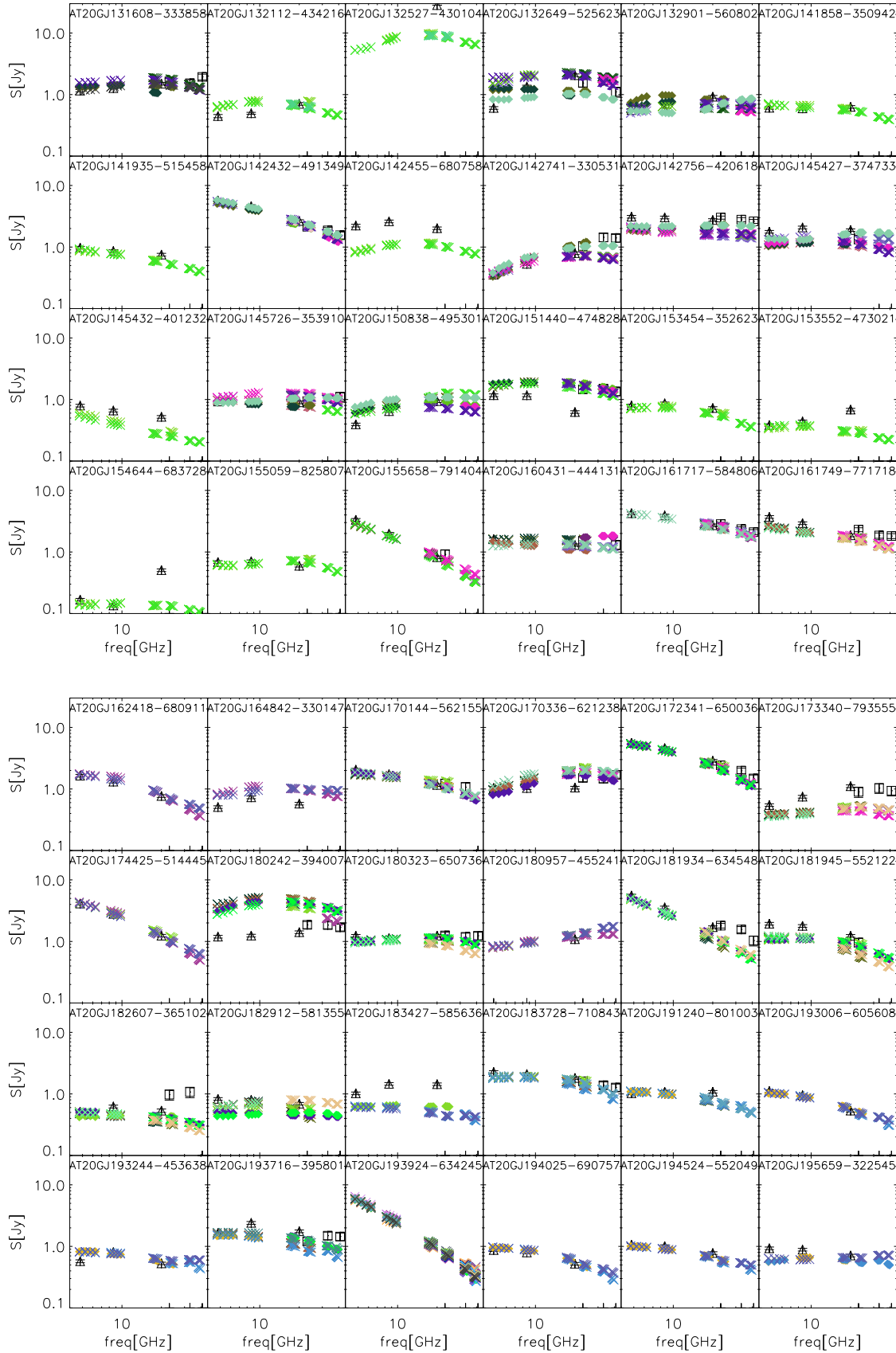


Figure 4. Continue.

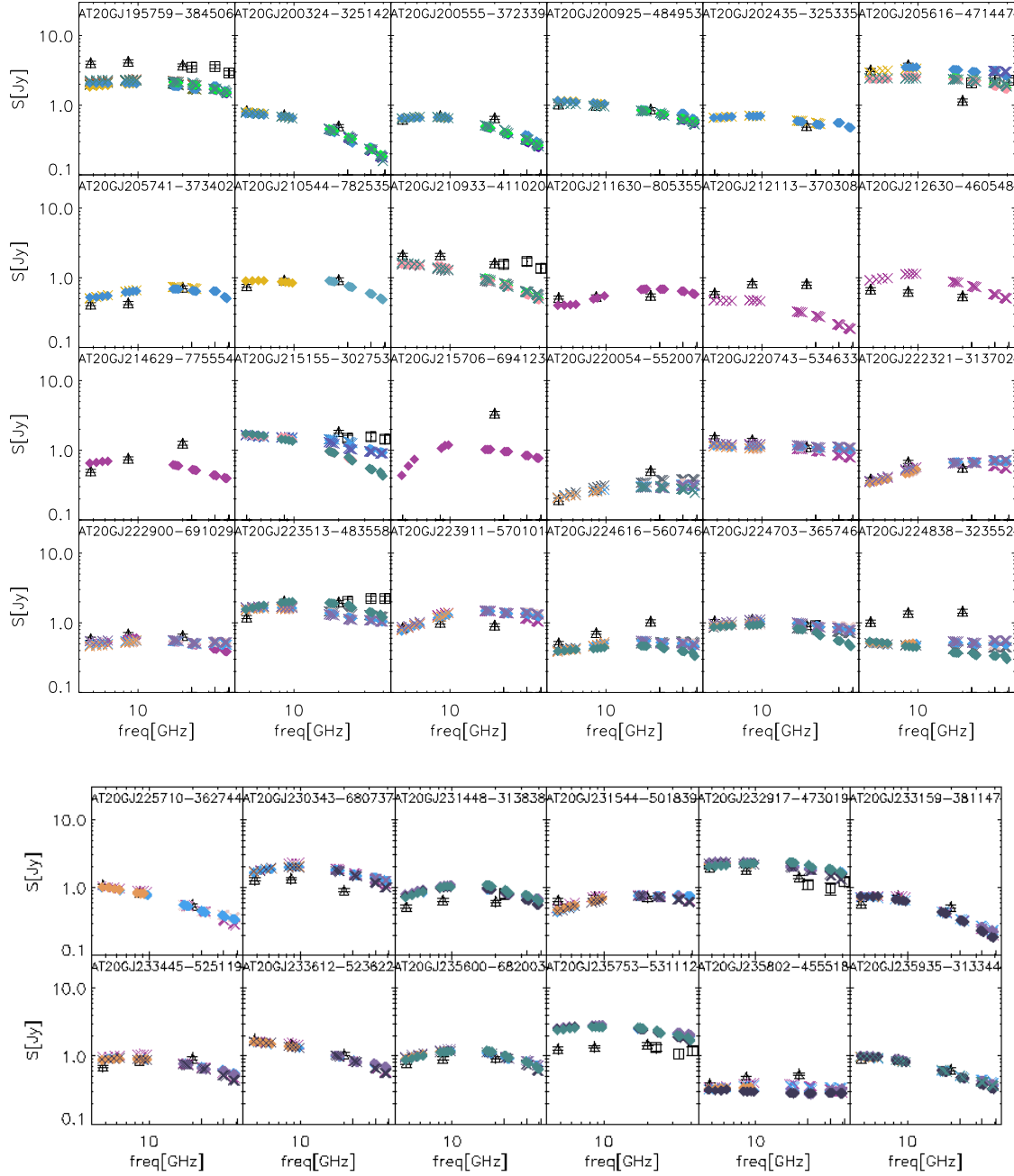


Figure 4. Continue.

3.1 Spectral behaviour

We have studied the spectra of our 174 *point-like* sources by fitting the observed data with a double power law:

$$S(\nu) = S_0 / [(\nu/\nu_0)^{-a} + (\nu/\nu_0)^{-b}], \quad (1)$$

where ν is the frequency in GHz, S the flux density in Jy and S_0 , ν_0 , a and b are free parameters. We considered only the sources for which we had at least 4 data points for each of the 2×2 GHz bands considered. The fit has been performed in logarithmic units by minimizing the χ^2 with a nonlinear optimization technique based on an implementation of the

Generalised Reduced Gradient optimisation method (GRG, Windward Technologies, 1997). The allowed ranges for the parameters are: $4.5 \leq \nu_0 \leq 40$, $a \geq -3$, $b \leq 3$. We have considered as bad fits those with $\chi^2 - \langle \chi^2 \rangle > 3\sigma_\chi$ where $\langle \chi^2 \rangle = 1.3$ and $\sigma_\chi = 0.54$ are mean and standard deviation of the Gaussian fit of the reduced χ^2 distribution of the fits over the whole PACO sample.

For 4 of the 174 sources we do not have enough data to obtain meaningful values of the parameters, while in 5 cases eq. (1) does not yield an acceptable fit (χ^2 above the threshold). For the remaining 165 sources we have classified

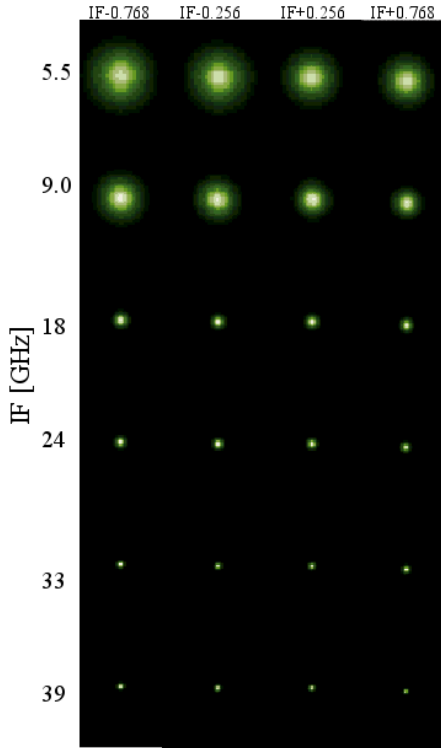


Figure 5. Images of the source AT20GJ053850-440508, observed on July 26th, 2009, as an example of the quality of our data and a representation of the beam. Each panel enclosing an image has a $6' \times 6'$ size. Rows show the images obtained in the four 512-MHz sub-bands associated to each of the 6 IFs.

the spectral shape according to the values of the low- and high-frequency spectral indices α_5^{10} and α_{30}^{40} ($S \propto \nu^\alpha$) defined in the ranges 5-10 GHz and 30-40 GHz and calculated using the fitting formula. The distribution of these spectral indices is shown in Fig. 6.

When $|\alpha_5^{10} - \alpha_{30}^{40}| < 0.35$ the source spectrum is classified as ‘single power law’. We have 19 such sources ($\simeq 11\%$), further subdivided in:

- 5 (2.9%) ‘steep’ with $\alpha_5^{10}, \alpha_{30}^{40} < -0.3$,
- 13 (7.6%) ‘flat’ with $|\alpha_5^{10}|, |\alpha_{30}^{40}| \leq 0.3$,
- 1 (0.6%) ‘inverted’ with $\alpha_5^{10}, \alpha_{30}^{40} > 0.3$.

The other 146 have been classified as follows (see Fig. 6):

- ‘peaked’ if $\alpha_5^{10} > 0.3, \alpha_{30}^{40} < -0.3$: 34 (20%) sources;
- ‘down-turning’ if $\alpha_{30}^{40} \leq \min(\alpha_5^{10} - 0.35, -\alpha_5^{10})$ and $\alpha_5^{10} \leq 0.3$: 104 sources (61%);
- ‘self-absorbed’ if $\alpha_5^{10} - 0.35 \geq \alpha_{30}^{40} \geq \max(-0.3, -\alpha_5^{10})$: 8 sources (4.7%).

Remarkably, we don’t find any ‘upturning’ source ($\alpha_5^{10} < \alpha_{30}^{40}$).

The peak frequency of ‘peaked’ sources is $\nu_p = \nu_0(-b/a)^{1/(b-a)}$. The distribution of ν_p in the observer frame is shown by the solid histogram in Fig. 7. The mean value is 17.3 GHz with a standard deviation of 4.5 GHz. The median is 15.6 GHz with inter-quartile range 14.0–20.5 GHz. The figure also shows the distribution of peak frequencies in the source frame for the 12 sources for which redshifts are available (Massardi et al. 2010, Mahony et al. in prep.). For

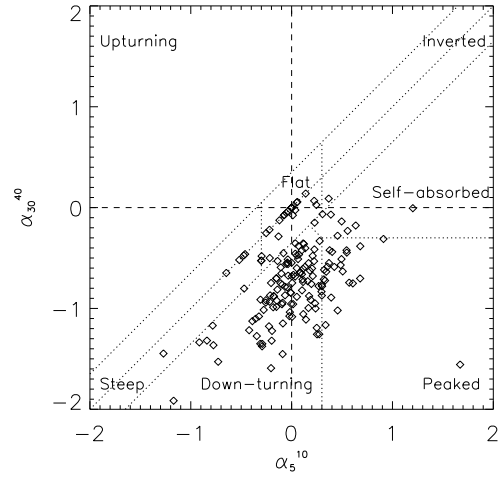


Figure 6. Colour-colour plot comparing the spectral indices in the ranges 5-10 and 30-40 GHz. The dotted lines shows the boundaries adopted for our spectral classification.

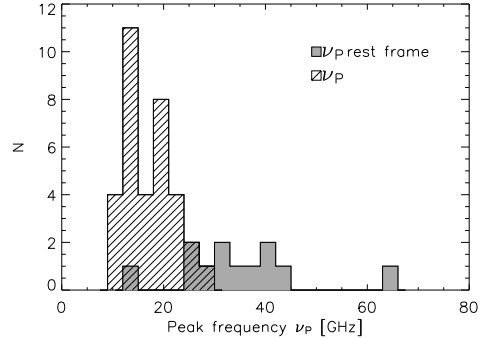


Figure 7. Distribution peak frequencies in the observer’s frame (hatched histogram) and in the source frame (shaded) for sources with measured redshift.

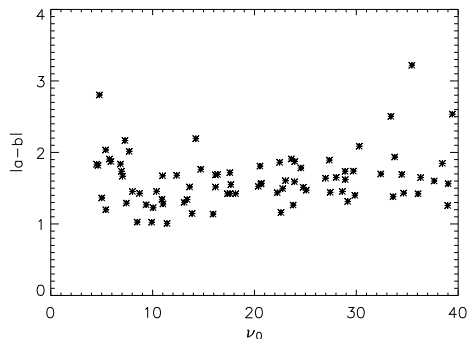


Figure 8. Absolute values of the variation of the slopes of down-turning sources as a function of the break frequency ν_0 [see eq. (1)].

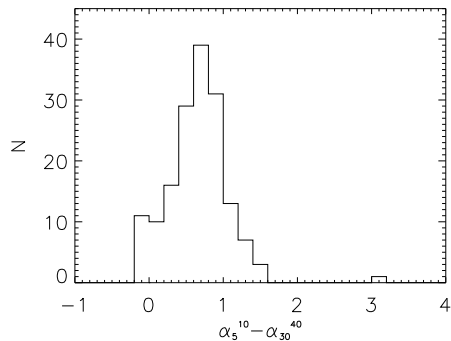


Figure 9. Distribution of the differences between low- and high-frequency spectral indices ($\alpha_5^{10} - \alpha_{30}^{40}$).

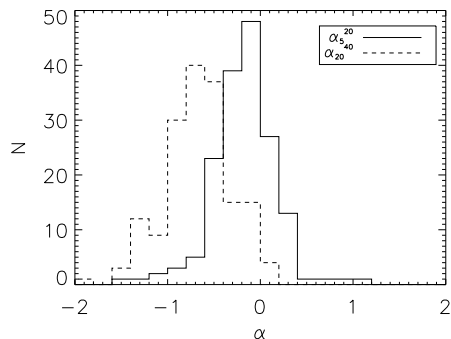


Figure 10. Distributions of spectral indices between 5 and 20 GHz (solid line) and between 20 and 40 GHz (dashed line).

these the median is 35.0 GHz with dispersion of 12.5 GHz; the median is 34.2 GHz with inter-quartile range is 27.7–39.9 GHz.

Figure 8 shows the distribution of the absolute values of the variation of slopes of down-turning sources as a function of the break frequency ν_0 [eq. (1)]. The two quantities appear to be uncorrelated. The distribution of ν_0 spans rather uniformly the full range of frequencies covered by PACO. The distribution of $|a - b|$ is quite narrow (mean = 1.63, st. dev. = 0.37, median = 1.50, first quart. = 1.42, third quart. = 1.81). The distribution of the differences between low- and high-frequency spectral indices ($\alpha_5^{10} - \alpha_{30}^{40}$) is shown in Fig. 9. There is a clear steepening of the spectra at high frequency. The mean difference is 0.76 with a standard deviation of 0.41. The median difference is 0.75 with inter-quartile range 0.52–1.02.

Even though a power-law is a poor description for the majority of the spectra, conventional spectral indices are still useful for practical purposes. For example, they provide the easiest way to extrapolate the observed counts or model predictions from one frequency to another. Figure 10 shows the distributions of spectral indices between 5 and 20 GHz and between 20 and 40 GHz (we refer to 20 GHz as the selection frequency of the PACO sample). The mean value of α_5^{20} is 0.1, with a standard deviation of 0.34, while the mean α_{20}^{40} is -0.57, with a standard deviation of 0.36. It should be noted, however, that the 20 GHz selection favours sources

Table 3. Median variability index of the bright sample at different frequencies and time lags.

Time range[d]	5.5 GHz	9 GHz	18 GHz	24 GHz	33 GHz	39 GHz
90	3.5	6.3	5.2	5.7	6.7	7.5
180	5.4	5.8	5.4	7.6	6.3	7.5
270	8.3	5.0	9.2	8.4	10.6	11.3

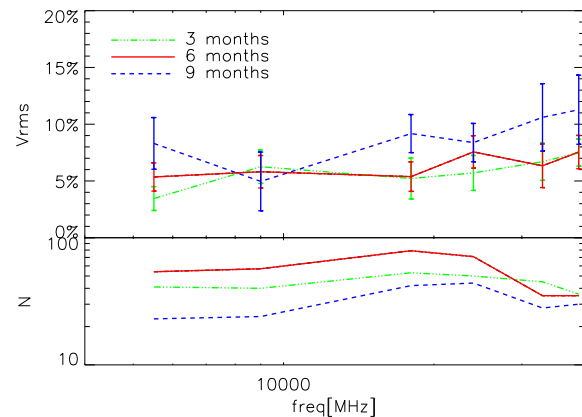


Figure 11. Top: median variability index of the sample as a function of frequency; error bars are $1.25\sigma/\sqrt{N-1}$. Bottom: number of sources.

that are brighter at this frequency. Therefore a positive value of $\alpha_5^{20} - \alpha_{20}^{40}$ is, at least partly, due to a selection effect.

3.2 Variability

Most of the sources in the sample have been observed more than once to monitor the flux density variations between the two Planck surveys. The time allocation scheme allowed us to have regular observations of a statistically significant sample on time scales of 6 months. The monitoring becomes increasingly incomplete for shorter and longer periods. Following Sadler et al. (2006) we define the variability index as:

$$V_{\text{rms}} = \frac{100}{\langle S \rangle} \sqrt{\frac{\sum [S_i - \langle S \rangle]^2 - \sum \sigma_i^2}{n}}$$

where S_i is the flux density of a given source measured at the i -th epoch, σ_i is the associated error, $n = 2$ is the number of measurements, and $\langle S \rangle$ is the mean flux density of the source, computed using all the available observations of the source (not only those used for computing the variability index).

To estimate the variability over a certain time interval we have selected for each source the best pair of observations spaced by the that time interval within $\pm 20\%$. In Fig 11 we show the median variability index for the sample of sources as a function of frequency for time intervals of 3, 6, and 9 months (upper panel) and the number of sources having pairs of observations for those time intervals (lower panel).

We find, as expected (Impey & Neugebauer 1988; Cia-

ramella et al. 2004), a trend toward an increase of the variability amplitude with frequency (see Table 3 and Fig. 11). There is also a marginal indication of higher variability for the longer time lag, consistent with earlier results (e.g. Ciarabella et al. 2004). Around 20 GHz the median variability index for a 9 months lag is $\simeq 9 \pm 1.7\%$, slightly larger than that found by Sadler et al. (2006) over a one year timescale (6.9%) for a somewhat fainter sample (flux density limit of 100 mJy). The distribution of V_{rms} , however, is similar to that found by Sadler et al.; for example, $37 \pm 9\%$ of our sources show a variability index larger than 10%, to be compared with $42 \pm 7\%$ for the Sadler et al. sample.

4 ABSOLUTE CALIBRATION FOR GROUND BASED TELESCOPES

The absolute calibration of the Planck detectors up to 353 GHz is derived from the annual modulation of the CMB dipole by the satellite orbit around the Sun. An absolute measurement of the dipole is obtained by differentiating along a spin period. The CMB dipole direction is expected to be recovered to better than ~ 2 arcmin, and its amplitude to better than 0.5% (The Planck collaboration 2006). Planck aims at obtaining an absolute photometric calibration better than 1% for all frequency channels up to 353 GHz. As discussed in López-Cañiego et al. (2007) the main limitation to the accuracy of flux density estimates of Planck sources is confusion due to faint sources within the beam. Leach et al. (2008) estimated typical rms errors ~ 100 mJy for the 30 and 44 GHz channels at high Galactic latitude. This corresponds to a few percent of the flux density of the brightest extragalactic sources.

Thus ground based observations, simultaneous with Planck's and at approximately the same frequencies, of very bright sources can be used to assess the absolute flux densities of calibrators for ground based telescopes. The PACO project has enough observations to determine the relative flux density scale between Planck and the ATCA.

Table 4 lists the 7 mm PACO flux densities of 6 compact sources with 20 GHz flux density $S_{\text{AT20G}} > 5$ Jy and high quality observations simultaneous to Planck's. With the exception of AT20GJ053850-440508, these sources lie outside the region covered by the bright sample. All of them are well-known highly variable blazars. Two of them are equatorial sources and are currently used in some ad-hoc observational runs for cross-calibration between Southern and Northern hemisphere telescopes, in order to assure that the Planck absolute calibration could be shared with all the major ground-based facilities. A comparison with Planck flux density scales will be done when Planck data will become available and will be partially presented with the first Planck data release (The Planck collaboration, in prep.).

5 CONCLUSIONS

The PACO project consists in observations with ATCA of several complete samples in three pairs of 2 GHz bands (5.5 and 9 GHz, 18 and 24 GHz, 33 and 39 GHz). The observations were carried out in several epochs between July 2009 and August 2010. At least one observation was made within

a week from the Planck satellite observations in any of the LFI channels (30, 44, 70 GHz).

Two complete flux-limited samples (a “bright sample” with $S_{20\text{GHz}} > 500$ mJy and a “faint sample” with $S_{20\text{GHz}} > 200$ mJy) were extracted from the AT20G catalogue (Murphy et al. 2010, Massardi et al. 2010). In addition we observed: a sample of sources with inverted or upturning spectra in the 5–20 GHz range; a sample of blazars included in a long-term monitoring program at SEST; a sample of ATCA calibrators.

We have presented and analyzed the data on sources in the “bright sample”. Although the present analysis is preliminary, in wait for the much broader spectral coverage that will be possible combining our measurements with Planck data, we note some interesting results:

- Only a minor fraction ($\simeq 11\%$) of source spectra have a shape close to a single power-law over the 4.5 to 40 GHz range; they are mostly “flat”-spectrum.
- Few sources have a positive (i.e. rising, $S \propto \nu^\alpha$) high-frequency (30 to 40 GHz) spectral index, and none has an upturning spectrum ($\alpha_{5\text{GHz}}^{10\text{GHz}} < \alpha_{30\text{GHz}}^{40\text{GHz}}$). Most sources show a spectral steepening above 10–20 GHz: the mean value of the spectral index is $\simeq 0.1$ (with a standard deviation of 0.34) between 5 and 20 GHz and decreases to $\simeq -0.57$ (with a standard deviation of 0.36) between 20 and 40 GHz. Break frequencies are almost uniformly distributed over the full frequency range covered by our observations. We do not find any correlation between the variation of the spectral index and the break frequency. We note that part of this steepening may be due to a selection effect since the primary 20 GHz selection of the sample emphasize sources which are brighter at this frequency.
- A significant fraction (about 20%) of the sources show a peak within our frequency range. The mean value of the peak frequency is 17.3 GHz with a standard deviation of 4.5 GHz. The mean rest frame peak frequency for the 12 such sources for which a redshift is available is 35.0 GHz with dispersion of 12.5 GHz. In general, however, the peak is not very prominent.
- A handful of sources (8, i.e. 4.7%) show a rising low-frequency spectrum, followed by a flattening, perhaps indicative of self-absorption up to $\simeq 10$ GHz.
- There is a trend toward an increase of the variability amplitude with frequency and a marginal indication of higher variability for the longer time lag.

We also present accurate flux density measurements, simultaneous with Planck, for 6 bright ($S_{\text{AT20G}} > 5$ Jy) point-like sources that can be used to exploit the excellent absolute calibration achieved by Planck to re-assess the high frequency calibration of ground-based telescopes and to improve models for planets and other sources used as calibrators at mm wavelengths.

On the other hand, our data will help in the validation of sources detected by Planck and in quantifying the effect of confusion on Planck flux density and position estimates.

ACKNOWLEDGMENTS

MM, AB, and GDZ acknowledge financial support for this research by ASI (ASI/INAF Agreement I/072/09/0 for the

Table 4. The 7 mm flux densities, measured simultaneously with Planck observations, of point-like calibrators in the PACO sample with $S_{\text{AT20G}} > 5 \text{ Jy}$. The figure immediately below each flux density measurement is the corresponding error.

AT20G name	RA [hr]	δ [deg]	Observing Date	$S_{32.2\text{GHz}}$ [mJy]	$S_{32.7\text{GHz}}$ [mJy]	$S_{33.2\text{GHz}}$ [mJy]	$S_{33.7\text{GHz}}$ [mJy]	$S_{38.2\text{GHz}}$ [mJy]	$S_{38.7\text{GHz}}$ [mJy]	$S_{39.2\text{GHz}}$ [mJy]	$S_{39.7\text{GHz}}$ [mJy]
				$\sigma_{S_{32.2\text{GHz}}}$ [mJy]	$\sigma_{S_{32.7\text{GHz}}}$ [mJy]	$\sigma_{S_{33.2\text{GHz}}}$ [mJy]	$\sigma_{S_{33.7\text{GHz}}}$ [mJy]	$\sigma_{S_{38.2\text{GHz}}}$ [mJy]	$\sigma_{S_{38.7\text{GHz}}}$ [mJy]	$\sigma_{S_{39.2\text{GHz}}}$ [mJy]	$\sigma_{S_{39.7\text{GHz}}}$ [mJy]
J053850-440508	5.6473226	-44.0858154	2010-02-28	9506	9483	9385	9356	8962	8921	8864	8893
				118	118	117	117	112	111	110	111
J053850-440508	5.6473226	-44.0858154	2010-03-15	14278	14210	14135	14137	14848	14620	14639	14814
				187	186	185	185	195	192	192	194
J053850-440508	5.6473226	-44.0858154	2009-09-15	6344	6352	6339	6339	6192	6156	6177	6141
				92	92	92	92	89	89	89	89
J125611-054721	12.9364349	-5.7893119	2010-07-16	14740	14665	14659	14659	14041	13956	14064	14089
				126	126	126	126	120	120	121	121
J133739-125724	13.6277171	-12.9568596	2010-07-16	4228	4197	4188	4181	3974	3955	3922	3876
				36	36	36	35	34	34	33	33
J183339-210341	18.5610881	-21.0611248	2009-09-26	3256	3210	3174	3132	2750	2714	2674	2639
				16	16	16	16	14	13	13	13
J192451-291430	19.4141825	-29.2417011	2010-04-01	17111	17807	17451	17748	0	0	0	0
				196	204	200	203	0	0	0	0
J192451-291430	19.4141825	-29.2417011	2010-04-10	14571	14696	14686	14357	14007	13782	13723	13891
				213	215	215	210	205	202	201	203
J192451-291430	19.4141825	-29.2417011	2009-09-26	14028	13876	13789	13663	12490	12393	12263	12127
				71	70	69	69	63	63	62	62
J192451-291430	19.4141825	-29.2417011	2009-10-07	15333	15248	15083	14820	14380	14225	14341	14617
				60	59	58	58	56	56	56	57
J192451-291430	19.4141825	-29.2417011	2009-10-14	13728	13641	13475	13267	12282	12179	12076	12078
				122	120	118	110	110	109	108	108
J222547-045701	22.4297933	-4.9503870	2009-11-06	6177	6098	5929	5905	5557	5337	5009	4978
				105	103	101	100	94	90	85	84
J222547-045701	22.4297933	-4.9503870	2009-11-19	5589	5524	5469	5417	4910	4840	4794	4743
				110	109	108	107	97	95	94	93

Planck LFI activity of Phase E2 and contract I/016/07/0 (COFIS). RDE acknowledges support of a Federation Fellowship (FF0345330).

We thank the staff at the Australia Telescope Compact Array site, Narrabri (NSW), for the valuable support they provide in running the telescope. The Australia Telescope Compact Array is part of the Australia Telescope which is funded by the Commonwealth of Australia for operation as a National Facility managed by CSIRO.

ety of the Pacific Conference Series, A Retrospective View of MIRIAD. pp 433–+

- The Planck Collaboration, 2006, arXiv:astro-ph/0604069
 Toffolatti L., Argüeso Gomez F., de Zotti G., Mazzei P., Franceschini A., Danese L., Burigana C., 1998, MNRAS, 297, 117
 Toffolatti L., De Zotti G., Argüeso F., Burigana C., 1999, ASPC, 181, 153
 Tornikoski M., et al., 1996, A&AS, 116, 157
 Windward Technologies, GRG2 Users's Guide, 1997

This paper has been typeset from a \TeX / \LaTeX file prepared by the author.

REFERENCES

- Burke-Spolaor S., Ekers R. D., Massardi M., Murphy T., Partridge B., Ricci R., Sadler E. M., 2009, MNRAS, 395, 504
 Ciaramella A., et al., 2004, A&A, 419, 485
 de Zotti G., Toffolatti L., Argüeso F., Davies R. D., Mazzotta P., Partridge R. B., Smoot G. F., Vittorio N., 1999, AIPC, 476, 204
 Eddington A. S., 1913, MNRAS, 73, 359
 Ferris, R.H., Wilson, W.E., 2002, URSI XXVIIth GA, Maastricht
 Hinshaw G. et al., 2007, Astrophysical Journal, Supplement, 170, 288
 Hogg D. W., 2001, AJ, 121, 1207
 Hogg D. W., Turner E. L., 1998, PASP, 110, 727
 Impey C. D., Neugebauer G., 1988, AJ, 95, 307
 Leach S. M., et al., 2008, A&A, 491, 597
 López-Caniego M., González-Nuevo J., Herranz D., Massardi M., Sanz J. L., De Zotti G., Toffolatti L., Argüeso F., 2007, ApJS, 170, 108
 Massardi M., Burigana C., 2010, NewA, 15, 678
 Massardi M., López-Caniego M., González-Nuevo J., Herranz D., de Zotti G., Sanz J. L., 2009, MNRAS, 392, 733
 Massardi M., et al., 2008, MNRAS, 384, 775
 Massardi M., et al., 2010, arXiv:1010.5942
 Murphy T. et al., 2010, Monthly Notices of the RAS, 402, 2403
 Sadler E. M. et al., 2006, Monthly Notices of the RAS, 371, 898
 Sault R. J., Teuben P. J., Wright M. C. H., 1995, in R. A. Shaw, H. E. Payne, & J. J. E. Hayes ed., Astronomical Data Analysis Software and Systems IV Vol. 77 of Astronomical Soci-